The Cryosphere Discuss., 8, 1673–1721, 2014
www.the-cryosphere-discuss.net/8/1673/2014/
doi:10.5194/tcd-8-1673-2014

The Cryosphere Discussions
Open Access

Elevation and elevation change of Greenland and Antarctica derived from CryoSat-2

V. Helm, A. Humbert, and H. Miller

Glaciology Section, Alfred Wegener Institute, Helmholtz Centre for Polar and Marine Research, Bremerhaven, Germany

Received: 1 February 2014 – Accepted: 5 March 2014 – Published: 25 March 2014

Correspondence to: V. Helm (veit.helm@awi.de)

Published by Copernicus Publications on behalf of the European Geosciences Union.

Abstract

The ESA satellite CryoSat-2 has been observing Earth's polar regions since April 2010. It carries a sophisticated radar altimeter and aims for the detection of changes in sea ice thickness as well as surface elevation changes of Earth's land and marine ice sheets. This study focuses on the Greenland and Antarctic ice sheets, considering the contemporary elevation of their surfaces. Based on 2 years of CryoSat-2 data acquisition, elevation change maps and mass balance estimates are presented. Additionally, new digital elevation models (DEMs) and the corresponding error maps are derived. Due to the high orbit of CryoSat-2 (88° N/S) and the narrow across-track spacing, more than 99 % of Antarctica's surface area is covered. In contrast, previous radar altimeter measurements of ERS1/2 and ENVISAT were limited to latitudes between 81.5° N and 81.5° S and to surface slopes below 1°. The derived DEMs for Greenland and Antarctica have an accuracy which is similar to previous DEMs obtained by satellite-based laser and radar altimetry (Liu et al., 2001; Bamber et al., 2009, 2013; Fretwell et al., 2013; Howat et al., 2014). Comparisons with ICESat data show that 80 % of the CryoSat-2 DEMs have an error of less than 3 m ± 30 m. For both ice sheets the surface elevation change rates between 2011 and 2012 are presented at a resolution of 1 km. Negative elevation changes are concentrated at the west and south-east coast of Greenland and in the Amundsen Sea embayment in West Antarctica (e.g. Pine Island and Thwaites glaciers). They agree well with the dynamic mass loss observed by ICESat between 2003 and 2008 (Pritchard et al., 2009). Thickening occurs along the main trunk of Kamb Ice Stream and in Dronning Maud Land. While the former is a consequence of an ice stream stagnated ~ 150 years ago (Rose, 1979; Retzlaff and Bentley, 1993), the latter represents a known large-scale accumulation event (Lenaerts et al., 2013). This anomaly partly compensates for the observed increased volume loss in West Antarctica. In Greenland the findings reveal an increased volume loss of a factor of 2 compared to the period 2003 to 2008. The combined volume loss of Greenland and Antarctica for the period 2011 and 2012 is estimated to be $-448 \pm 122\,\mathrm{km^3\,yr^{-1}}$.

TCD
8, 1673–1721, 2014

1 Introduction

Ice sheet surface topography is of interest to glaciologists for several reasons. For example, the observation of changes in surface elevation represents, in an integrative way, the response of an ice sheet to changes in ice dynamics and surface mass balance. A digital elevation model (DEM) is an important input boundary condition for numerical flow modelling, while elevation changes estimates can serve as a validation for prognostic models simulating the recent evolution of ice sheets. Other applications are wide-ranging: from field campaign planning to the estimation of driving stresses to applications in InSAR processing, a technique widely used to derive mass balance estimates of glaciers and ice streams. To improve the InSAR mass balance estimates, an accurate and contemporary DEM is needed to distinguish between topography and ice motion, both contributing to the interferometric phase difference between two SAR acquisitions.

Observation of ice surface elevation can be achieved by operating satellite or airborne altimeters using laser or radar signals. In order to assess volume changes, and consequently the mass balance of ice sheets, a continuous survey of the ice surface elevation is of high importance. The newest, and since the loss of ENVISAT only, satellite-borne altimeter with ice applications is CryoSat-2, which was launched in April 2010. CryoSat-2's core instrument, the Synthetic Aperture Interferometric Radar Altimeter (SIRAL), samples the surface every 300 m along-track using three different measurement modes, LRM, SAR and SARIn. The low-resolution mode (LRM), used over oceans and the flat interior of the ice sheets, is a conventional pulse-limited radar altimeter integrating the backscattered energy over the full beam width resulting in a footprint of roughly 15 km. However, the pulse-limited footprint, which is used for the elevation detection, is only about 2.5 km in diameter. In the synthetic aperture (SAR) and synthetic aperture interferometric (SARIn) modes the along-track footprint is decreased to 300 m by using the Doppler history in the SAR processing of the coherent Ku-band radar altimeter system. SAR is used over sea ice to reveal ice freeboard by

TCD
8, 1673–1721, 2014

distinguishing leads and ice flows, whereas SARIn measures the steeper areas at the margins of the ice sheets and ice caps. In SARIn a second antenna is mounted across the flight track direction. This enables the point of closest approach (POCA) to be identified using interferometric processing.

ESA provides calibrated SAR processed CryoSat data as a level 1B product, including the satellite position, the backscattered radar echoes, geophysical corrections and quality flags. For the study a threshold first maxima re-tracker (TFMRA) was developed to precisely determine the range to the POCA. Subsequently, corrections for datation, path delays (e.g. atmospheric refraction) and tides for floating ice masses were applied.

For the DEM generation the Baseline B product of a full 369-day-long cycle, from January 2012 to January 2013, was used. The processing, illustrated in Fig. 1, is split into two lines, one for LRM and one for SARIn. In the SARIn line next to the radar echo, the coherence and the differential phase between the two antennas are used to determine the range and the direction to the POCA. In the LRM line the range is re-tracked; this is followed by an iterative approach to determine the slope correction using an a priori input DEM and the relocation method. After each iteration a new DEM is generated and used as the input DEM in the next iteration step. Finally, all SARIn and LRM geo-referenced surface elevations are interpolated using ordinary kriging to obtain DEMs in three different resolutions and different search radii.

For validation purposes and estimation of uncertainties, comparisons with data from satellite- and airborne laser altimeters were made. Data from the Geoscience Laser Altimeter System (GLAS) on board NASA's Ice, Cloud, and land Elevation Satellite (ICESat) were used. Uncertainty maps were generated using an updated multi regression approach.

Maps of elevation change, hereinafter referred to as $\mathrm{d}h/\mathrm{d}t$, are generated by comparing two full cycles of CryoSat-2 data acquired between January 2011 and January 2013 using an along-track processing approach. All $\mathrm{d}h$ estimates were scaled to a $\mathrm{d}t$ of 1 year. Finally a block median was applied to achieve a 1 km grid resolution for Greenland and Antarctica using a 50 km search radius.

TCD
8, 1673–1721, 2014

A detailed technical description of the data processing for the different products is given below and in Appendix A5.

2 New digital elevations models of Greenland and Antarctica

In the following two new DEMs of Greenland and Antarctica and their uncertainty maps are presented. A total of 7.5×10^6 and 61×10^6 radar echoes for Greenland and Antarctica are used in the processing, respectively. Both final DEMs are regular grids with a resolution of 1 km × 1 km. Only CryoSat-2 data were used in the processing. This prevents influences from inter-mission offsets which are difficult to determine. Due to the short acquisition time period of 1 year, effects introduced by recent elevation changes are reduced. For example, the most recent DEM of Antarctica published in 2013 is a composite of radar altimeter data of ERS1 acquired in 1994 and laser altimeter data acquired between 2003 and 2008 (Fretwell et al., 2013).

ICESat provides high-accuracy surface topography data up to 86.0° S/N with coarse across-track spacing (25 km at 70° and 40 km at 60°), and ERS1 is limited to 81.5° S/N with narrow across-track spacing (2 km at 70° and 4 km at 60°) but less accuracy in sloped terrain. In contrast, CryoSat-2 provides data up to 88.0° S/N with narrow across-track spacing of 2.5 km, at 70° and 4 km at 60°, which is similar to ERS1, and due to the newly developed SAR Interferometric Radar Altimeter (SIRAL) instrument carried by CryoSat-2, the accuracy in sloped terrain is higher than ERS1.

Three different grids are derived using different search radii. The search radius is the area around each grid cell where data points are collected for the kriging interpolation (Isaaks and Srivastava, 1989; Deutsch and Journel, 1992). To reduce processing time, not more than the 80 closest points are used. The grids are the following: first – 1 km grid resolution using a search radius of 6 km; second – 10 km grid resolution using a search radius of 50 km; and third – 25 km grid resolution using a 250 km search radius. Finally, gaps in the 1 km grid are filled by the re-sampled 10 km grid. Data gaps occur if less than three data points are found in one of the eight sectors of each

TCD
8, 1673–1721, 2014

search radius. This methodology should prevent a unidirectional weighting along-track and guarantee a uniform weighting in the interpolation, since data coverage along-track is very high but can be sparse across-track. The across-track distance increases with lower latitude, and due to the interferometric processing, large data gaps occur in areas of steep across-track slope, e.g. at the flanks of ice domes. Here, retrieved POCA elevations are concentrated at the ridges. In areas close to the grounding line or where range tracker loss occurred due to mountainous or rough terrain, such as experienced over the Antarctic Peninsula, less data coverage and hence large interpolation errors can be expected.

To fill the pole hole around the South Pole (> 88° S), the re-sampled 25 km grid is used. Older sparse cartographic data sets to fill the pole hole were disclaimed, since they show errors of several hundreds of metres in the flat area between 88° S and 86° S.

The DEM of Antarctica represented in Fig. 2 covers an area of nearly 14 M km^2, including ice shelves and the South Pole. In the corresponding slope map in Fig. 3 the ice divides in East Antarctica are well represented. Even larger subglacial lakes such as Lake Vostok are visible in this logarithmic colour-scaled, continent-wide slope distribution. The derived slope map is in agreement with previous studies (Fretwell et al., 2013) and show only minor differences in the low sloped areas and, as expected, higher differences of up to 0.3° in steeper terrain. Furthermore, the slope direction is in very good agreement with the DEM of Fretwell et al. (2013), and therefore the ice divide positions do not differ significantly.

In Figs. 4 and 5 the Greenland DEM and its corresponding slope map are respectively presented. Ice divides in central Greenland are well pronounced. Slopes increase towards the margins and exceed values of 2° at the ice edge.

DEM accuracy

To retrieve the accuracy of the two CryoSat DEMs, decimetre-precise laser spot measurements from ICESat were used. Uncertainty maps are generated using 2×10^6 for

TCD
8, 1673–1721, 2014

Greenland and 22×10^6 for Antarctica ICESat surface elevation points of the laser campaigns L3F, L3G and L3H, acquired in June 2006, November 2006 and March/April 2007, respectively. Before the comparison several corrections were applied to the ICESat data of processing version GLA12.033 (for details see Appendix A4). The elevation of the DEM at the laser footprint location was obtained using bilinear interpolation. Differences are investigated qualitatively and as a function of surface slope, retrieved from the two DEMs. To estimate the uncertainty induced by the interpolation method (ordinary kriging), cross-point analysis of the input CryoSat-2 data set with the ICESat data was performed. The uncertainty introduced by ICESat is determined from intra-mission crossover analysis of ICESat L3G campaign data over the whole Antarctic continent. As is shown in Fig. 6, the accuracy of the DEM and the CryoSat data themselves are slope-dependent, and thus degrading with higher slopes. However, the ICESat data show almost no slope dependency. The mean difference was found to be 0.01 m with a standard deviation of 0.65 m (46 748 crossovers). Outliers of several metres are found in mountainous and crevassed areas and at locations where clouds could not be filtered out. Those findings are in agreement with reports of the GLAS engineering team and others (Bamber and Gomez-Dans, 2005; Shuman et al., 2006; Brenner et al., 2007; Shi et al., 2008). On the basis of this result it can be assumed that uncertainties in the ICESat data set are negligible and hence can be used as the reference data set.

Over 30, 82 and 96 % of Antarctica has surface slopes of less than 0.1, 0.5, and 1.5°, respectively. Therefore, the analysis is restricted to slopes of less than 1.5°. In Fig. 6 the blue diamonds show the median difference and standard deviation σ of CryoSat data and ICESat at inter-mission crossovers plotted as a function of surface slope at intervals of 0.01°. In the same figure the red diamonds represent the ICESat intra-mission crossover difference, indicating the high accuracy of the reference data. To avoid uncertainties inserted by elevation changes occurring between 2007 and 2012, the ICESat data set was corrected using the ICESat elevation change map derived in this study, assuming a constant elevation change. It is evident that for low slopes (< 0.1°), representing more than a third of the Antarctic ice sheet, the median difference of

TCD
8, 1673–1721, 2014

CryoSat-2 to ICESat is less than 0.2 m with an uncertainty, σ, of less than 1.5 m. Even for higher slopes of 1° the median difference is below 3 m with σ of less than 5 m. The black diamonds in Fig. 6 also indicate that the main component of the uncertainty of the DEM is generated by the interpolation algorithm, despite the dense data coverage of CryoSat. The median difference of the DEM to ICESat as well as σ increase with increasing slope. However, 90 % of DEMs differ not more than 3.5 m, with a σ of less than 15 m. For the remaining 10 %, the accuracy decreases to 13 m with a σ of 70 m. Large uncertainties occur in mountainous areas such as the Transantarctic Mountain range; the Heimefrontjella in Dronning Maud Land; the catchment area of Amery Ice Shelf, Antarctic Peninsula; and at the rocky margins around Greenland. Errors below 1 m are found in the dry snow zone of Greenland, at ice domes and divides, ice shelves and also at Lake Vostok. A comparison with the latest elevation model of Antarctica (Fretwell et al., 2013) reveals differences of less than 10 m for 80 % of the whole area. Larger offsets of up to 100 m are seen in the mountainous areas, at the edges of ice caps and ice ridges close to the coast, and from the South Pole to 86° S. The latter is caused by low-quality cartographic data south of 86° S (Fretwell et al., 2013), whereas CryoSat-2 delivers data up to 88° S.

Due to the high data coverage of CryoSat, the Greenland DEM show more detailed surface patterns, especially in southern Greenland, than an older DEM which is based on ICESat data only (DiMarzio et al., 2007). However, the most recent high-resolution DEM of Greenland, produced within the Greenland Ice Mapping Project (GIMP) by Howat et al. (2014), is outperforming the CryoSat DEM. Differences between ICESat data points and the CryoSat DEM are less than 4 m with uncertainties of up to 52 m for areas of less than 1°. This corresponds to approximately 75 % of the area of Greenland. Especially the margins of Greenland, with its surrounding rocks, mountains and steep valleys, are not well represented and showed differences to ICESat data points of more than 7 m with high uncertainties of up to 80 m. In contrast, the GIMP DEM differs compared to ICESat data points by less than 2 m, with uncertainties not more

TCD
8, 1673–1721, 2014

than 40 m all over Greenland. A comparison of the CryoSat DEM with the GIMP DEM revealed a mean difference of less than 1 m ± 82 m for areas inside the GIMP ice mask.

Comparison with airborne laser scanner data (LSC) from the Alfred Wegener Institute and data of NASA's Airborne Topographic Mapper Instrument (ATM) and NASA's Land, Vegetation, and Ice Sensor (LVIS), acquired between 2010 and 2012 during the Operation Ice Bridge (OIB) missions, reveals reliable elevation of the new DEMs even in larger catchment areas at the margins. Results of the comparisons are presented in Table 1, where laser data from various kind of surfaces are compared against the new CryoSat DEMs and previous published DEMs for Greenland (Howat et al., 2014) and Antarctica (Fretwell et al., 2013). For all sites, situated in low sloped areas, the CryoSat DEMs show good accuracy with biases of less than 1 m. Uncertainties range from 0.2 m for Dome C and the North Eemian drilling site in northwestern Greenland (NEEM) to up to 45 m in the dry snow zone in Greenland (elevations above 2200 m) and the area south of 85° S. Even in areas of higher but gentle slope, e.g. Law Dome and Halvfaryggen in Dronning Maud Land, Antarctica, reveal differences of less than 0.5 m with uncertainties of 12 m and 29 m, respectively. The high uncertainties of Halvfaryggen can be explained by high interpolation errors due to data loss at the grounding line. Larger offset of 4 to 5 m with uncertainties of up to 133 m are found in the more rough and sloped margins of Greenland (area below 2200 m) and Antarctica (e.g. blue ice area close to the Schirmacher Oasis in Dronning Maud Land).

3 Ice surface elevation change

Ice surface elevation change estimates based on altimetry data have been presented in the past in regional and global studies. Changes at the margins of Greenland and Antarctica based on ICESat data were presented by Pritchard et al. (2009). The strength of ICESat is its high single point and repeat track accuracy (usually within 2 km), as well as a small footprint (70 m) resulting in low slope-induced errors (Fricker, 2005; Shuman et al., 2006; Brenner et al., 2007). However, laser measurements are

TCD
8, 1673–1721, 2014

always affected by clouds and might be disturbed by drifting snow, causing data gaps and interrupted time series. Furthermore the large across-track spacing prohibits observations of small-scale spatial patterns. Radar altimeter measurements of ERS1/2 and ENVISAT were limited to latitudes between 81.5° S and 81.5° N and to surface slopes below 1°. The benefit of CryoSat-2, however, is not only a dense track spacing and small pole hole but also the possibility of measurements in areas of larger slopes due to the new interferometric SAR system. This enables continuous observations where elevation change is most rapid, namely along the relatively steep and narrow margins of the ice sheets as well as larger glaciers and ice caps. Radar is not affected by cloud coverage, and time series of elevation change can be generated using the along-track method (Pritchard et al., 2009; Flament and Rémy, 2012). The technical details of the estimation of $\mathrm{d}h/\mathrm{d}t$ are presented in Appendix A5.

The following presents the first elevation change maps of Antarctica (Fig. 7) and Greenland (Fig. 8) derived from CryoSat-2 data acquired in 2011 and 2012. In total 3×10^6 and $28.5 \times 10^6 \mathrm{d}h/\mathrm{d}t$ values are used to derive the elevation change maps for Greenland and Antarctica, respectively. An updated along-track method (see Appendix A5), attending to the drifting orbit and the large POCA displacement in sloped and rough regions is used. This allows for spatial patterns of elevation change in catchment areas to be resolved. This technique successfully reproduces the large-scale patterns of ice sheet change in both Antarctica and Greenland. Prominent in Antarctica is the strong dynamical thinning in the Amundsen Sea embayment (up to $10\,\mathrm{m\,yr^{-1}}$), Totten Glacier in East Antarctica and some large glaciers of the Antarctic Peninsula (Fig. 7). Dynamical thickening of the stagnated Kamb Ice Stream is of the same order as presented previously (Pritchard et al., 2009). An extended area was found in Dronning Maud Land, East Antarctic Ice Sheet, where thickening of up to $1.0\,\mathrm{m\,yr^{-1}}$ takes place. The thickening decreases inland, but still reaches values of 0.1 to 0.2 m on the plateau. It represents an accumulation anomaly reported previously (Lenaerts et al., 2013; Boening et al., 2012). This anomaly is very unusual in its spatial extent and magnitude and has a large impact on the mass balance of Antarctica, as presented

TCD
8, 1673–1721, 2014

below. In situ observations confirm the increase in accumulation rate. At the automatic weather station DK190 (76.794° S, 31.9° E; 3741 m a.s.l.) 200 km apart from Dome Fuji, the anomaly exceeds the annual accumulation rate of 34.1 kg m^{-2} yr^{-1} (Fujita et al., 2011) by 30 % (S. Fujita and S. Kipfstuhl, personal communication, 2014). The remaining parts of the plateau do not show any significant elevation change.

Prominent in Greenland is the strong thinning of the entire western ice sheet, as well as the south-east and north-west ice sheet margins, as shown in Fig. 8. The dynamic thinning of Jakobshavn Isbræ in particular has penetrated deep into the ice sheet. Thinning of the Zacharias Isstrømen, an outlet glacier of the North East Greenland Ice Stream (NEGIS), show rates of 1.0 m yr^{-1} at the glacier terminus. This thinning extends 250 km upstream of the NEGIS, where values of 0.2–0.3 m yr^{-1} have been reported. Joughin et al. (2010) showed an increase in speed and retreat of the terminus of Zacharias Isstrømen. Although this outlet glacier was previously reported to have a negative mass balance (Rignot and Kanagaratnam, 2006), this pattern of pronounced thinning is a new development (Khan et al., 2014, in press).

The interior of Greenland does not exhibit a significant change. Slight thickening is also seen inland of the north-west coast of Greenland (up to 45° W) as well as in the higher areas in southern Greenland. Thickening reaches values of maximum 0.25 m yr^{-1}, also reported previously by Pritchard et al. (2009) with the same rate.

3.1 Comparison of dh/dt estimates

A comparison of recent elevation change were carried out between data from CryoSat 2011/2012 and ICESat from 2004 to 2008. For both altimeters the same along-track technique was applied for Greenland and Antarctica including the interior of Antarctica up to 86°. Verification of the along-track-processing technique was executed by applying it to ICESat data and cross-checking it with previous studies. This showed the same pattern as Pritchard et al. (2009) and confirms the estimates of Scott et al. (2009), which gives additional confidence in the robustness of the algorithm used. A subsequent comparison of dh/dt from 2011 and 2012 derived from CryoSat to dh/dt seen

TCD
8, 1673–1721, 2014

by ICESat 2004–2008 exhibits the accumulation anomaly described earlier, as well as the continued and increased thinning of ice in West Greenland and the Amundsen Sea Embayment.

3.2 Areas of large elevation changes

In the following two prominent regions with large surface elevation change are presented, namely Jakobshavn Isbræ and Pine Island Glacier (PIG). Figure 9 reveals that the pattern of thinning corresponds with the location of the PIG tributaries. Thinning of the tributaries reaches far upstream and exceeds values of $1\,\mathrm{m\,yr^{-1}}$. Also, areas with flow velocities as low as $100\,\mathrm{m\,yr^{-1}}$ are affected. Thinning rates are in agreement with other studies reporting accelerated thinning of the order of 0.1 to $0.2\,\mathrm{m\,a^{-2}}$, (e.g. Scott et al., 2009; Wingham et al., 2009; Flament and Rémy, 2012). Figure 9 displays the Pine Island Glacier catchment basin, a subset of the CryoSat $\mathrm{d}h/\mathrm{d}t$ grid, overlayed by the CryoSat measurements as dark-grey dots, ICESat as black dots and the three GPS sites (Scott et al., 2009) as yellow hexagons. Table 2 presents the comparison to the findings of Scott et al. (2009) at the in situ GPS sites. The two upstream GPS sites (PC111 and PC171) show higher elevation change rates with CryoSat than with ICESat. Assuming a linear acceleration of the elevation change rate over the last 5 years, the increase is determined to be $0.15\,\mathrm{m\,a^{-2}}$ for the two upstream sites. At site PC55, which is located downstream, the CryoSat estimates equal those of ICESat. Observed differences might reflect a change of the dynamics of PIG, or may also be caused by interpolation artefacts since the closest ICESat data point is approximately 10 km apart the PC55 site, whereas is it much closer for PC111 and PC171 (2 km). At all sites the GPS measured elevation change in 2007 is almost twice that of the ICESat observed change for the same period. This offset might be caused by the spatial averaging (median filtering) applied in the processing, leading to an underestimation of local maxima. Therefore, it is assumed that the CryoSat results give more conservative estimates of recent elevation change.

TCD
8, 1673–1721, 2014

The second example is Jakobshavn Isbræ (Fig. 10), which has accelerated to speeds of ~ 16 km yr^{-1} Joughin et al. (2010) after its floating tongue disintegrated in 2003. Thinning was previously reported by Thomas et al. (2003); Csatho et al. (2008). Thinning rates observed in 2011–12 exceeded 4 m yr^{-1}. This thinning is most pronounced in the lower part of both tributaries, but extends 250 km upstream. This value is lower than values published previously and a rather conservative estimate that is influenced by the strong spatial averaging. Actual values exceed this rate: for example, Hurkmans et al. (2012b) reported values of up to 17 m yr^{-1}.

4 Conclusions

DEMs of Antarctica and Greenland are derived from one full cycle of CryoSat-2 data over the period from January 2012 to 2013. They are presented with an error of less than 3.5 m ± 15 m for Antarctica and 5 m ± 65 m for Greenland in approximately 90 % of the area of the ice sheets. The differences to previous DEMs are small; however, in Antarctica improvements can be seen in the area between 86° S and 88° S. The CryoSat-2 data processing was done by applying a newly developed re-tracker and an iterative approach for the slope correction, as well as the new interferometric processing of the SARIn data. Based on two cycles of CryoSat-2 data the combined volume loss of both ice sheets for the period 2011 and 2012 is estimated to be -448 ± 122 km^3 yr^{-1}. In Table 3 the volume rates are listed; these indicate that Greenland is contributing -353 ± 29 km^3 yr^{-1}, which is nearly 80 % of the total loss. This is an increase by a factor of 2 compared to values estimated for the period 2003 to 2008 (Sørensen et al., 2011; Shepherd et al., 2012) and mirrors the findings of Tedesco et al. (2013), who reported a mass loss record in 2011/2012 of -575 ± 95 Gt yr^{-1}. In Antarctica the volume loss for the period 2011 and 2012 is estimated to be -96 ± 93 km^3 yr^{-1}. Similar to Greenland margins, West Antarctica is observing an increase in volume loss. Compared to the period 2003 to 2008, the loss increased from -25 to -188 ± 11 km^3 yr^{-1}. Furthermore, the results clearly demonstrate

TCD
8, 1673–1721, 2014

that accumulation events on a large spatial scale and short temporal scale, as observed in Dronning Maud Land, are partly compensating for the increasing volumes loss.

This sheds new light on the temporal evolution of volume change and consequently mass change of the ice sheets and raises the question of on which timescale sea level change responds to yearly mass imbalances of the ice sheets, as well as how regional sea level observations will capture this. To answer those questions it is important to continue the measurement of elevation change using advanced technologies such as CryoSat-2 and to extend time series of elevation change dating back to the early 1990s. Furthermore, it is imperative to extend the operational CryoSat-2 data acquisition as long as possible since it is currently the only remaining altimeter system observing polar regions since the loss of ICESat in 2009 and ENVISAT in 2011. This will bridge the the gap until the launch of ICESat-2 in 2017.

The complete set of grids are available in geotiff format from the lead author (V. Helm) and will be provided on the data server PANGAEA (http://www.pangaea.de). Users will be notified of new releases as they become available.

Appendix A

A1 CryoSat-2 data processing

This study is based on LRM and SARIn level 1B CryoSat data distributed by the ESA. The level 1B contains precise orbit, waveforms and flags of additional information, such as geophysical and tidal corrections as well as bad data flags. For the dh/dt processing additional Baseline B data covering February 2011 to December 2012 were added. For the DEM generation, Baseline B data from a full cycle (369 days) were used, starting January 2012. Firstly, the general processing includes a waveform filter. Initially this identifies "bad waveforms" generated in rough or steep terrain when either the internal

TCD
8, 1673–1721, 2014

range tracker loses track or waveforms have no clear leading edge, e.g. due to high surface roughness. Secondly, the range is determined using a threshold first maxima re-tracker (TFMRA) developed for this study to ensure the best possible re-tracking method for observing elevation changes. Davis (1997) suggested that for determining elevation changes, the most accurate approach is to use a threshold re-tracker focusing on the lower part of the leading edge and thus the surface scattering part. This ensures that spatial or temporal changes in the extinction coefficient of the snow influencing mainly the volumetric component of the waveform do not influence the elevation measurement. An example is shown in Fig. 11, where in East Antarctica, a periodic pattern is observed at crossovers of ascending and descending tracks. Results obtained with the ESA standard, the NASA GSFC (NASA, 2006), the OCOG (using a threshold of 0.25 of the OCOG amplitude) (Wingham et al., 1986) and the modified TFMRA (using a threshold of 0.25 of the first maxima) are shown in panels a–d, respectively. The origin of this static pattern is likely to be caused by prominent wind fields at the East Antarctic Plateau (Armitage et al., 2013). However, the results of this study show that one can avoid a correction for the static "Antarctic pattern" in dh/dt estimates when using an appropriate re-tracker.

For LRM a threshold of 0.25 of the normalized maximum of the first maximum of the echo was used. The SARIn waveforms are re-tracked in combination with the coherence and phase difference included in the level 1B product. After re-tracking the range is corrected for delays caused by the atmospheric refraction (ionosphere, wet and dry troposphere), solid earth and pole tides. Data over the ice shelves around Antarctica are corrected for ocean loading and ocean tides. Additionally, tidal corrections are applied using the model CATS2008a (Padman et al., 2002, 2008). It is important to note that the corrections for the inverse barometric effect were applied to all data points falling within the CATS2008a model extensions which are based on grounding lines derived from MODIS-based Mosaic of Antarctica (MOA) images (Haran et al., 2005) with updates from InSAR in a few places, notably the SE Ross Ice Shelf (L. Padman, personal communication, 2013). This is necessary since the surface-type flags in the

TCD
8, 1673–1721, 2014

CryoSat-2 data product are imprecise, as will be shown in Appendix A5. Finally, a correction is applied for the dating bias, since LRM data are biased by −4.7 ms (Scagliola and Fornari, 2013). The filtered elevation product is then used as input for the DEM and dh/dt production.

A2 DEM generation

For DEM generation, an iterative approach was utilized following the processing scheme presented in Fig. 1. LRM and SARIn processing are decoupled, since the slope correction is achieved in a different way. Slope correction means that the echo position is shifted up slope towards the point of closest approach (POCA). Depending on the surface slope this correction can be of the order of several kilometres (Brenner et al., 1983). For LRM a first DEM is generated using the filtered input data set. Then the slope correction is applied to each data point using the relocation method described in Roemer et al. (2007). A second DEM is generated with the slope-corrected data set replacing the first one. This iterative process is repeated four times, improving the estimates with each iteration. In the SARIn processing line the slope correction is derived from the phase difference at the re-tracked position. The coherence is used as additional quality control. A similar procedure as presented by Galin et al. (2013) to obtain the POCA using the re-tracked phase difference were used. In the final step all slope-corrected LRM and SARIn data are used to generate the final gridded DEMs using ordinary kriging.

A3 Uncertainty of the DEM

To derive the uncertainty map the approach previously published by Griggs and Bamber (2009) was followed with some modifications. ICESat elevations of the three campaigns 3F, 3G and 3H served as reference data. As a first step the difference between the DEM and the reference data set is taken at the ICESat position using bilinear interpolation. Based on the assumption that the uncertainty depends on the surface

TCD
8, 1673–1721, 2014

roughness, the surface slope, the number of data points (N) used for interpolation and its variance (SD), additional factors of surface slope, roughness, N and SD at each ICESat position were derived from the corresponding raster data sets. Slope and roughness rasters are directly obtained from the DEM. N is determined by counting all data points lying closer than a radius R to each grid cell and SD is the standard deviation of those points. R is set to 6 km, the radius which was used for the DEM generation. Subsequently, all the differences are divided into 100 bins with an increment of 0.02° (slope), 0.12 m (SD), 0.05 m (roughness) and 10 points (N). For each increment the median and mean, as well as the standard deviation, is determined. To each of the contributions a higher order polynomial of the order of 8 is fitted. This includes any measurement errors (ME) which are low at low slope, low roughness, low SD and large N (coefficients are listed in Tables 4 and 5). ME are derived from the corresponding standard deviations of each bin. This kind of weighting and the high polynomial order ensures small residuals of the fit in bins with a small ME, reflecting areas of low slope such as flat ice sheet interiors. As a final step the polynomial coefficients together with the four raster data sets are used to derive four independent uncertainty grids. Finally, a combined uncertainty grid is determined using a weighted average of the four grids, presented for Antarctica and Greenland in Figs. 12 and 13, respectively. The weighting factors are gained from standard deviation of the residuals between data and polynomial fit (see Tables 4 and 5). Higher weights are given to the uncertainty raster with less discrepancy to the data. Hence, the uncertainty of the DEM is then given as

$$\sigma_h = \sum_{i=1}^{4} W_i \sigma_i, \tag{A1}$$

with

$$\sigma_i = C_0 + C_1 x + C_2 x^2 + c_3 x^3 + C_4 x^4 + C_5 x^5 + C_6 x^6 + C_7 x^7 + C_8 x^8; \tag{A2}$$

TCD
8, 1673–1721, 2014

W_i is the weighting factor and i is the independent source of uncertainty ($i = 1$ is the slope, $i = 2$ the standard deviation of h within one grid cell, $i = 3$ the roughness, and $i = 4$ the number of points N within one grid cell).

A4 ICESat data processing

ICESat data set GLA12 release 33 (Zwally et al., 2011) was used for this study. All surface elevations were referenced to WGS84 and corrected for saturation and an error in the range determination from transmit-pulse reference selection (centroid vs. Gaussian, G–C) (Zwally, 2013; Borsa et al., 2013). A cloud filter was applied using internal data flags with thresholds given in Pritchard et al. (2009) and Kwok et al. (2007). The inter-campaign offsets were determined for the release 33 data following Ewert et al. (2012) and are listed in Table 6 (H. Ewert, personal communication, 2013).

A5 Method for deriving dh/dt

Before deriving elevation change estimates the full data sets of Baseline A and Baseline B are processed as described in Appendix A1 and illustrated in Fig. 14. To prevent an underestimation of the basin-integrated volume change (Hurkmans et al., 2012), the two re-tided (replacement of tide model) LRM data sets are slope-corrected using the new DEMs. For determining elevation changes, a method which differs slightly from published ones (Pritchard et al., 2009; Smith et al., 2009; Sørensen et al., 2011; Flament and Rémy, 2012) was applied: due to the relocation slope correction method, the elevation measurements are shifted towards the POCA and are therefore offset from the reference track. Consequently, a reference track cannot be used for the determination of closest data points. Instead, for each data point in year 1, all respective neighbours in year 2 within a 1000 m distance were determined. From this subset the elevation rates ($\mathrm{m\,yr^{-1}}$) between the single year 1 and all valid year 2 measurements are determined using elevation and acquisition time. One has to consider that the elevation rates are disturbed by topography in sloped regions. For example, a point 1 km

TCD
8, 1673–1721, 2014

apart from another part in a 0.1° sloped area is 1.75 m higher in elevation. Hence, it is necessary to correct every single dh/dt measurement for the topography using a DEM. Finally, all dh/dt values larger than ±20 m are rejected, and to further reduce the uncertainty an iterative 2-σ filter is applied (two filter steps). The resulting data points are averaged. This procedure is repeated for each year 1 measurement. The final dh/dt data set (comprising of all averaged points) are gridded to rasters with 1 km spacing using a block median and a search radius of 50 km. Again, for each grid cell the same iterative 2-σ filter is applied to reduce the uncertainty. Finally, an uncertainty grid is generated using a Gaussian error propagation described below. With this method an uncertainty estimate based on the elevation change measurement itself can be derived. In contrast, Pritchard et al. (2009) and Scott et al. (2009) found a constant uncertainty of 0.07 m yr^{-1}, whereas Shepherd et al. (2012) used the observed 5-year variability of Antarctic accumulation fluctuations of the long-term mean accumulation rate as basis for estimating the uncertainty of volume (mass) change.

A6 Error estimation of dh/dt

The approach to determine the elevation change $\dot{h}$ is based on the following equation:

$$\dot{h} = \frac{\mathrm{d}h}{\mathrm{d}t} = \frac{1}{N}\sum_{i=1}^{N}\frac{h_i - h_{\mathrm{ref}}}{t_i - t_{\mathrm{ref}}}; \tag{A3}$$

h_{ref} represents the elevation measurement in year 1, whereas h_i are the N year 2 neighbours lying within 1000 m distance. Furthermore, the influence of the local topography is corrected using the new DEM:

$$\dot{h} = \frac{\mathrm{d}h - \mathrm{d}h_{\mathrm{DEM}}}{\mathrm{d}t} = \frac{1}{N}\sum_{i=1}^{N}\frac{(h_i - h_{\mathrm{ref}}) - \left(h_{\mathrm{DEM}_i} - h_{\mathrm{DEM}_{\mathrm{ref}}}\right)}{t_i - t_{\mathrm{ref}}}. \tag{A4}$$

TCD
8, 1673–1721, 2014

From Eq. (A4) the uncertainty $\sigma_{\dot{h}}$ is obtained using Gaussian error propagation:

$$\sigma_{\dot{h}} = \frac{1}{N}\sqrt{\sum_{i=1}^{N}\left(\frac{\mathrm{d}\dot{h}}{\mathrm{d}h_i}\right)^2\sigma_{h_i}^2 + \left(\frac{\mathrm{d}\dot{h}}{\mathrm{d}h_{\mathrm{ref}}}\right)^2\sigma_{h_{\mathrm{ref}}}^2 + \left(\frac{\mathrm{d}\dot{h}}{h_{\mathrm{DEM}_i}}\right)^2\sigma_{\mathrm{DEM}_i}^2 + \left(\frac{\mathrm{d}\dot{h}}{h_{\mathrm{DEM}_{\mathrm{ref}}}}\right)^2\sigma_{\mathrm{DEM}_i}^2}. \quad \text{(A5)}$$

The error terms $\sigma_{h_i} = \sigma_{h_{\mathrm{ref}}}$ are the uncertainty of a single elevation measurement. This is a contribution of uncertainties in orbit, radar speckle, re-tracking and geophysical corrections. The orbit is known to be better than 0.03 m; radar speckle is estimated in Wingham et al. (2006a) to be 0.16 m; and the geophysical corrections, including the ionosphere and the dry and wet troposphere, are in total within 0.04 m over the ice sheets (E. Schrama, personal communication, 2014). The uncertainty added through re-tracking is assumed to be 0.2 m, which is around half the sampling interval of the radar echoes. Consequently, σ_{h_i} was set to $\sigma_{h_i} = 0.3$ m.

The error terms of the topographic correction are directly related to the quality of the DEM. Therefore the formerly derived error map of the DEM and bilinear interpolation was used to determine σ_{DEM_i} and $\sigma_{\mathrm{DEM}_{\mathrm{ref}}}$.

The final gridded uncertainty map of the gridded $\dot{h}$ product is obtained using Gaussian error propagation of the mean value of all $\dot{h}$ values lying within 50 km distance of each grid cell:

$$\sigma_{\underline{\dot{h}}} = \frac{1}{N}\sqrt{\sum_{i=1}^{N}\sigma_{\dot{h}_i}^2}. \quad \text{(A6)}$$

The resulting uncertainty maps of elevation change ($\sigma_{\underline{\dot{h}}}$) are shown for both ice sheets in Figs. 15 and 16, respectively.

Acknowledgements. The German Ministry of Economics and Technology (grant 50EE1008 to V. Helm) have supported this work. We thank Heiko Ewert (TU Dresden) for providing the inter-campaign offsets of ICESat. Furthermore, we thank Robert Cullen and Marco Fonari from ESA

TCD
8, 1673–1721, 2014

for their support in issues regarding the quality of CryoSat-2 data. Laurence Padman and Lana Erofeeva kindly provided the tide model CATS and supported us in the evaluation of issues at the grounding line.

References

Angelen, J., Broeke, M., Wouters, B., and Lenaerts, J.: Contemporary (1960–2012) evolution of the climate and surface mass balance of the Greenland Ice Sheet, Surv. Geophys., 1–20, doi:10.1007/s10712-013-9261-z, 2013.

Armitage, T., Wingham, D., and Ridout, A.: Meteorological origin of the static crossover pattern present in low-resolution-mode CryoSat-2 data over Central Antarctica, IEEE Geosci. Remote S., 11, 1295–1299, doi:10.1109/LGRS.2013.2292821, 2013. 1687

Bamber, J. and Gomez-Dans, J. L.: The accuracy of digital elevation models of the Antarctic continent, Earth Planet. Sc. Lett., 237, 516–523, doi:10.1016/j.epsl.2005.06.008, 2005. 1679

Bamber, J. L., Gomez-Dans, J. L., and Griggs, J.: Antarctic 1 km Digital Elevation Model (DEM) from combined ERS-1 radar and ICESat laser satellite altimetry, 2009. 1674

Bamber, J. L., Griggs, J. A., Hurkmans, R. T. W. L., Dowdeswell, J. A., Gogineni, S. P., Howat, I., Mouginot, J., Paden, J., Palmer, S., Rignot, E., and Steinhage, D.: A new bed elevation dataset for Greenland, The Cryosphere, 7, 499–510, doi:10.5194/tc-7-499-2013, 2013. 1674

Boening, C., Lebsock, M., Landerer, F., and Stephens, G.: Snowfall-driven mass change on the East Antarctic ice sheet, Geophys. Res. Lett., 39, L21501, doi:10.1029/2012GL053316, 2012. 1682

Borsa, A. A., Moholdt, G., Fricker, H. A., and Brunt, K. M.: A range correction for ICESat and its potential impact on ice sheet mass balance studies, The Cryosphere Discuss., 7, 4287–4319, doi:10.5194/tcd-7-4287-2013, 2013. 1690

Brenner, A., DiMarzio, J., and Zwally, H.: Precision and accuracy of satellite radar and laser altimeter data over the continental ice sheets, IEEE T. Geosci. Remote, 45, 321–331, doi:10.1109/TGRS.2006.887172, 2007. 1679, 1681

Brenner, A. C., Bindschadler, R. A., Thomas, R. H., and Zwally, H. J.: Slope-induced errors in radar altimetry over continental ice sheets, J. Geophy. Res., 88, 1617–1623, 1983. 1688

Church, J., Clark, P., Cazenave, A., Gregory, J., Jevrejeva, S., Levermann, A., Merrifield, M., Milne, G., Nerem, R., Nunn, P., Payne, A., Pfeffer, W. T., Stammer, D., and Unnikrishnan, A.:

TCD
8, 1673–1721, 2014

Sea level change, in: Climate Change 2013: The Physical Science Basis. Contribution of Working Group I to the Fifth Assessment Report of the Intergovernmental Panel on Climate Change, edited by: Stocker, T. F., Qin, D., Plattner, G.-K., Tignor, M., Allen, S. K., Boschung, J., Nauels, A., Xia, Y., Bex, V., and Midgley, P. M., Tech. rep., Cambridge University Press, Cambridge, UK, New York, NY, USA, 2013.

Csatho, B., Schenk, T., Van Der Veen, C., and Krabill, W. B.: Intermittent thinning of Jakobshavn Isbræ, West Greenland, since the Little Ice Age, J. Glaciol., 54, 131–144, doi:10.3189/002214308784409035, 2008. 1685

Davis, C.: A robust threshold retracking algorithm for measuring ice-sheet surface elevation change from satellite radar altimeters, IEEE T. Geosci. Remote, 35, 974–979, doi:10.1109/36.602540, 1997. 1687

Deutsch, C. V. and Journel, A.: GSLIB: Geostatistical Software Library and User's Guide, Oxford University Press, New York, 1992. 1677

DiMarzio, J., Brenner, A., Schutz, R., Shuman, C. A., and Zwally, H. J.: GLAS/ICESat 1 km laser altimetry digital elevation model of Greenland, 2007. 1680

Ewert, H., Popov, S. V., Richter, A., Schwabe, J., Scheinert, M., and Dietrich, R.: Precise analysis of ICESat altimetry data and assessment of the hydrostatic equilibrium for subglacial Lake Vostok, East Antarctica, Geophys. J. Int., 191, 557–568, doi:10.1111/j.1365-246X.2012.05649.x, 2012. 1690, 1705

Flament, T. and Rémy, F.: Dynamic thinning of Antarctic glaciers from along-track repeat radar altimetry, J. Glaciol., 58, 830–840, doi:10.3189/2012JoG11J118, 2012. 1682, 1684, 1690

Fretwell, P., Pritchard, H. D., Vaughan, D. G., Bamber, J. L., Barrand, N. E., Bell, R., Bianchi, C., Bingham, R. G., Blankenship, D. D., Casassa, G., Catania, G., Callens, D., Conway, H., Cook, A. J., Corr, H. F. J., Damaske, D., Damm, V., Ferraccioli, F., Forsberg, R., Fujita, S., Gim, Y., Gogineni, P., Griggs, J. A., Hindmarsh, R. C. A., Holmlund, P., Holt, J. W., Jacobel, R. W., Jenkins, A., Jokat, W., Jordan, T., King, E. C., Kohler, J., Krabill, W., Riger-Kusk, M., Langley, K. A., Leitchenkov, G., Leuschen, C., Luyendyk, B. P., Matsuoka, K., Mouginot, J., Nitsche, F. O., Nogi, Y., Nost, O. A., Popov, S. V., Rignot, E., Rippin, D. M., Rivera, A., Roberts, J., Ross, N., Siegert, M. J., Smith, A. M., Steinhage, D., Studinger, M., Sun, B., Tinto, B. K., Welch, B. C., Wilson, D., Young, D. A., Xiangbin, C., and Zirizzotti, A.: Bedmap2: improved ice bed, surface and thickness datasets for Antarctica, The Cryosphere, 7, 375–393, doi:10.5194/tc-7-375-2013, 2013. 1674, 1677, 1678, 1680, 1681, 1700

TCD
8, 1673–1721, 2014

Fricker, H. A.: Assessment of ICESat performance at the salar de Uyuni, Bolivia, Geophys. Res. Lett., 32, L21S06, doi:10.1029/2005GL023423, 2005. 1681

Fujita, S., Holmlund, P., Andersson, I., Brown, I., Enomoto, H., Fujii, Y., Fujita, K., Fukui, K., Furukawa, T., Hansson, M., Hara, K., Hoshina, Y., Igarashi, M., Iizuka, Y., Imura, S., Ingvander, S., Karlin, T., Motoyama, H., Nakazawa, F., Oerter, H., Sjöberg, L. E., Sugiyama, S., Surdyk, S., Ström, J., Uemura, R., and Wilhelms, F.: Spatial and temporal variability of snow accumulation rate on the East Antarctic ice divide between Dome Fuji and EPICA DML, The Cryosphere, 5, 1057–1081, doi:10.5194/tc-5-1057-2011, 2011. 1683

Galin, N., Wingham, D. J., Cullen, R., Fornari, M., Smith, W. H. F., and Abdalla, S.: Calibration of the CryoSat-2 interferometer and measurement of across-track ocean slope, IEEE T. Geosci. Remote, 51, 57–72, doi:10.1109/TGRS.2012.2200298, 2013. 1688

Griggs, J. A. and Bamber, J. L.: A new 1 km digital elevation model of Antarctica derived from combined radar and laser data – Part 2: Validation and error estimates, The Cryosphere, 3, 113–123, doi:10.5194/tc-3-113-2009, 2009. 1688

Haran, T., Bohlander, J., Scambos, T., and Fahnestock, M.: MODIS mosaic of Antarctica (MOA) image map, Digital media, National Snow and Ice Data Center, Boulder, CO, USA, 2005. 1687

Howat, I. M., Negrete, A., and Smith, B. E.: The Greenland Ice Mapping Project (GIMP) land classification and surface elevation datasets, The Cryosphere Discuss., 8, 453–478, doi:10.5194/tcd-8-453-2014, 2014. 1674, 1680, 1681, 1700

Hurkmans, R. T. W. L., Bamber, J. L., and Griggs, J. A.: Brief communication "Importance of slope-induced error correction in volume change estimates from radar altimetry", The Cryosphere, 6, 447–451, doi:10.5194/tc-6-447-2012, 2012a. 1690

Hurkmans, R. T. W. L., Bamber, J. L., Sørensen, L. S., Joughin, I. R., Davis, C. H., and Krabill, W. B.: Spatiotemporal interpolation of elevation changes derived from satellite altimetry for Jakobshavn Isbræ, Greenland, J. Geophys. Res.-Earth, 117, F03001, doi:10.1029/2011JF002072, 2012b. 1685

Isaaks, E. H. and Srivastava, R. M.: An Introduction to Applied Geostatistics, Oxford University Press, New York, 1989. 1677

Joughin, I., Smith, B. E., Howat, I. M., Scambos, T., and Moon, T.: Greenland flow variability from ice-sheet-wide velocity mapping, J. Glaciol., 56, 415–430, doi:10.3189/002214310792447734, 2010. 1683, 1685

TCD
8, 1673–1721, 2014

Khan, S., Kjaer, K., Bevis, M., Bamber, J., Wahr, J., Kjeldsen, K., Bjørk, A., Korsgaard, N., Stearns, L., van den Broeke, M., Liu, L., Larsen, N., and Muresan, I.: Sustained mass loss of the Northeast Greenland ice sheet triggered by regional warming, Nature Climate Change, doi:10.1038/nclimate2161, 2014. 1683

Kwok, R., Cunningham, G. F., Zwally, H. J., and Yi, D.: Ice, Cloud, and land Elevation Satellite (ICESat) over Arctic sea ice: retrieval of freeboard, J. Geophys. Res., 112, C12013, doi:10.1029/2006JC003978, 2007. 1690

Lenaerts, J. T. M., van Meijgaard, E., van den Broeke, M. R., Ligtenberg, S. R. M., Horwath, M., and Isaksson, E.: Recent snowfall anomalies in Dronning Maud Land, East Antarctica, in a historical and future climate perspective, Geophys. Res. Lett., 40, 2684–2688, doi:10.1002/grl.50559, 2013. 1674, 1682

Liu, H., Jezek, K. C., Li, B., and Zhao, Z.: Radarsat Antarctic Mapping Project Digital Elevation Model Version 2, Digital media, National Snow and Ice Data Center, Boulder, CO, USA, 2001. 1674

NASA: NASA GSFC Retracking Algorithms, http://icesat4.gsfc.nasa.gov/radar_data/data_processing/gsfcretrackdoc.960725.php (last access: 16 October 2013), 2006. 1687

Padman, L., Fricker, H. A., Coleman, R., Howard, S., and Erofeeva, L.: A new tide model for the Antarctic ice shelves and seas, Ann. Glaciol., 34, 247–254, doi:10.3189/172756402781817752, 2002. 1687

Padman, L., Erofeeva, S. Y., and Fricker, H. A.: Improving Antarctic tide models by assimilation of ICESat laser altimetry over ice shelves, Geophys. Res. Lett., 35, L21501, doi:10.1029/2008GL035592, 2008. 1687

Peltier, W.: Global glacial isostasy and the surface of the ice-age earth: the ICE-5G (VM2) model and GRACE, Annu. Rev. Earth Pl. Sc., 32, 111–149, doi:10.1146/annurev.earth.32.082503.144359, 2004.

Pritchard, H. D., Arthern, R. J., Vaughan, D. G., and Edwards, L. A.: Extensive dynamic thinning on the margins of the Greenland and Antarctic ice sheets, Nature, 461, 447–558, doi:10.1038/nature08471, 2009. 1674, 1681, 1682, 1683, 1690, 1691

Retzlaff, R. and Bentley, C. R.: Timing of stagnation of Ice Stream C, West Antarctica, from short-pulse radar studies of buried surface crevasses, J. Glaciol., 39, 553–561, 1993. 1674

Rignot, E. and Kanagaratnam, P.: Changes in the velocity structure of the Greenland Ice Sheet, Science, 311, 986–990, 2006. 1683

TCD
8, 1673–1721, 2014

Roemer, S., Legresy, B., Horwath, M., and Dietrich, R.: Refined analysis of radar altimetry data applied to the region of the subglacial Lake Vostok/Antarctica, Remote Sens. Environ., 106, 269–284, 2007. 1688

Rose, K.: Characteristics of ice flow in Marie Byrd Land, Antarctica, J. Glaciol., 24, 63–75, 1979. 1674

Scagliola, M. and Fornari, M.: Known biases in CryoSat Level1b products, Tech. rep., ESA, 2013. 1688

Scott, J. B. T., Gudmundsson, G. H., Smith, A. M., Bingham, R. G., Pritchard, H. D., and Vaughan, D. G.: Increased rate of acceleration on Pine Island Glacier strongly coupled to changes in gravitational driving stress, The Cryosphere, 3, 125–131, doi:10.5194/tc-3-125-2009, 2009. 1683, 1684, 1691, 1701, 1714

Shepherd, A., Ivins, E. R., A, G., Barletta, V. R., Bentley, M. J., Bettadpur, S., Briggs, K. H., Bromwich, D. H., Forsberg, R., Galin, N., Horwath, M., Jacobs, S., Joughin, I., King, M. A., Lenaerts, J. T. M., Li, J., Ligtenberg, S. R. M., Luckman, A., Luthcke, S. B., McMillan, M., Meister, R., Milne, G., Mouginot, J., Muir, A., Nicolas, J. P., Paden, J., Payne, A. J., Pritchard, H., Rignot, E., Rott, H., Sørensen, L. S., Scambos, T. A., Scheuchl, B., Schrama, E. J. O., Smith, B., Sundal, A. V., van Angelen, J. H., van de Berg, W. J., van den Broeke, M. R., Vaughan, D. G., Velicogna, I., Wahr, J., Whitehouse, P. L., Wingham, D. J., Yi, D., Young, D., and Zwally, H. J.: A reconciled estimate of ice-sheet mass balance, Science, 338, 1183–1189, doi:10.1126/science.1228102, 2012. 1685, 1691, 1702

Shi, H., Lu, Y., Bao, L., Du, Z., and Zhang, Z.: 2003–2008 ice sheet elevation change on the Lake Vostok, Antarctica, from ICESat, in: Education Technology and Training, 2008, and 2008 International Workshop on Geoscience and Remote Sensing, ETT and GRS 2008, 21–22 December 2008, Shanghai, China, vol. 2, 561–564, doi:10.1109/ETTandGRS.2008.279, 2008. 1679

Shuman, C. A., Zwally, H. J., Schutz, B. E., Brenner, A. C., DiMarzio, J. P., Suchdeo, V. P., and Fricker, H. A.: ICESat Antarctic elevation data: preliminary precision and accuracy assessment, Geophys. Res. Lett., 33, L07501, doi:10.1029/2005GL025227, 2006. 1679, 1681

Smith, B. E., Fricker, H. A., Joughin, I. R., and Tulaczyk, S.: An inventory of active subglacial lakes in Antarctica detected by ICESat (2003–2008), J. Glaciol., 55, 573–595, doi:10.3189/002214309789470879, 2009. 1690

Sørensen, L. S., Simonsen, S. B., Nielsen, K., Lucas-Picher, P., Spada, G., Adalgeirsdottir, G., Forsberg, R., and Hvidberg, C. S.: Mass balance of the Greenland ice sheet (2003–2008)

TCD
8, 1673–1721, 2014

from ICESat data – the impact of interpolation, sampling and firn density, The Cryosphere, 5, 173–186, doi:10.5194/tc-5-173-2011, 2011. 1685, 1690

Tedesco, M., Fettweis, X., Mote, T., Wahr, J., Alexander, P., Box, J. E., and Wouters, B.: Evidence and analysis of 2012 Greenland records from spaceborne observations, a regional climate model and reanalysis data, The Cryosphere, 7, 615–630, doi:10.5194/tc-7-615-2013, 2013. 1685

Thomas, R. H., Abdalati, W., Frederick, E., Krabill, W. B., Manizade, S., and Steffen, K.: Investigation of surface melting and dynamic thinning on Jakobshavn Isbrae, Greenland, J. Glaciol., 49, 231–239, doi:10.3189/172756503781830764, 2003. 1685

Whitehouse, P. L., Bentley, M. J., Milne, G. A., King, M. A., and Thomas, I. D.: A new glacial isostatic adjustment model for Antarctica: calibrated and tested using observations of relative sea-level change and present-day uplift rates, Geophys. J. Int., 190, 1464–1482, doi:10.1111/j.1365-246X.2012.05557.x, 2012.

Wingham, D. J., Rapley, C. G., and Griffiths, H.: New techniques in satellite altimeter tracking systems, in: Proceedings of the IGARSS Symposium, vol. SP-254, 1339–1344, edited by: Guyenne, T. D. and Hunt, J. J., European Space Agency, Zurich, September 1986, 1986. 1687

Wingham, D., Francis, C. R., Baker, S., Bouzinac, C., Cullen, R., de Chateau-Thierry, P., Laxon, S. W., Mallow, U., Mavrocordatos, C., Phalippou, L., Ratier, G., Rey, L., Rostan, F., Viau, P., and Wallis, D.: CryoSat: a mission to determine the fluctuations in earth's land and marine ice fields, Adv. Space Res., 37, 841–871, 2006a. 1692

Wingham, D. J., Shepherd, A., Muir, A., and Marshall, G. J.: Mass balance of the Antarctic ice sheet, Philos. T. R. Soc. A, 364, 1627–35, doi:10.1098/rsta.2006.1792, 2006b.

Wingham, D. J., Wallis, D. W., and Shepherd, A.: Spatial and temporal evolution of Pine Island Glacier thinning, 1995 to 2006, Geophys. Res. Lett., 36, L17501, doi:10.1029/2009GL039126, 2009. 1684

Zwally, H. J.: Correction to the ICESat data product surface elevations due to an error in the range determination from transmit-pulse reference-point selection (Centroid vs Gaussian), Tech. rep., NSIDC, http://nsidc.org/data/icesat/correction-to-product-surface-elevations.html (last access: 12 November 2013), 2013. 1690

Zwally, H. J., Schutz, R., Bentley, C., Bufton, J., Herring, T., Minster, J., Spinhire, J., and Thomas, R.: GLAS/ICESat L2 Antarctic and Greenland Ice Sheet Altimetry Data, Version 33,

TCD
8, 1673–1721, 2014

[GLA12], available at: http://nsidc.org/data/gla12.html (last access: 25 March 2013), 2011. 1690
Zwally, H. J., Giovinetto, M. B., Beckley, M. A., and Saba, J. J. L.: Antarctic and Greenland Drainage Systems, available at: http://icesat4.gsfc.nasa.gov/cryo_data/ant_grn_drainage_systems.php (last access: 16 January 2014), 2012.

TCD
8, 1673–1721, 2014

Table 1. Comparison of airborne laser altimetry data with the new CryoSat DEMs and the GIMP DEM for Greenland (Howat et al., 2014) and Bedmap2 DEM for Antarctica (Fretwell et al., 2013). Laser data were acquired with the NASA Airborne Topographic Mapper instrument and/or the Land Vegetation and Ice Sensor (LVIS) during Operation Ice Bridge (OIB) missions by NASA. Laser scanner data (LC) were acquired by the Alfred Wegener Institute (AWI) using a RIEGL LMS VQ-560 instrument.

Region	Data	Date	Difference to CryoSat (m)	Difference to GIMP/Bedmap2 (m)	*N* points
Raster (30 km × 50 km) GRE (NEEM)	LSC AWI	2010	−0.3 ± 0.22	−0.08 ± 0.92	1 883 711
OIB all over GRE (above 2200 m)	ATM NASA	2012	−0.01 ± 45.0	−0.25 ± 27.0	2 088 058
OIB all over GRE (below 2200 m)	ATM NASA	2012	3.95 ± 133.6	1.97 ± 21.80	4 519 748
Four 70 km long tracks ANT (Halvfaryggen)	LSC AWI	2012	0.3 ± 29.0	1.1 ± 44.0	2 087 648
Star-like pattern 20 km ANT (Dome C)	LSC AWI	2012	−0.6 ± 0.17	−1.3 ± 0.32	347 988
Raster (20 km × 40 km) ANT (Law Dome)	LSC AWI	2012	−0.1 ± 12.0	2.8 ± 6.0	1 322 915
Raster (20 km × 30 km) ANT (blue ice)	LSC AWI	2012	5.0 ± 7.0	1.6 ± 20.0	1 791 050
OIB ICESat validation ANT (south of 85° S)	LVIS NASA	2009	0.6 ± 39.4	0.7 ± 74.3	1 605 224
OIB ICESat validation ANT (south of 85° S)	LVIS NASA	2010	0.08 ± 11.7	1.95 ± 33.5	1 561 916

TCD
8, 1673–1721, 2014

Table 2. Elevation change ($m yr^{-1}$) at GPS points from Scott et al. (2009) at Pine Island Glacier.

	PC55	PC111	PC171
2003–2007 ICESat (Scott et al., 2009)	−1.9 ± 0.4	−1.0 ± 0.4	−0.6 ± 0.4
2006/2007 GPS (Scott et al., 2009)	−3.5 ± 0.65	−2.0 ± 0.4	−1.2 ± 0.2
2004–2008 ICESat (this study)	−2.3 ± 0.0	−1.2 ± 0.0	−0.7 ± 0.0
2011–2012 CryoSat (this study)	−2.0 ± 0.0	−1.7 ± 0.0	−1.4 ± 0.0

TCD
8, 1673–1721, 2014

Table 3. Volume rate estimates of this study compared with ICESat from IMBIE (Shepherd et al., 2012).

Region	Area (Mio km^2)	IMBIE 2003–2008 dV/dt (km^3 yr^{-1})	CryoSat 2011–2012 dV/dt (km^3 yr^{-1})
GrIS	1.68	-189 ± 20	-352 ± 29
APIS	0.22	-28 ± 11	-30 ± 15
EAIS	9.74	$+78 \pm 19$	$+122 \pm 67$
WAIS	1.74	-25 ± 7	-188 ± 11
AIS	11.71	$+25 \pm 12$	-96 ± 93
GrIS + AIS	13.39	-164 ± 32	-448 ± 122

TCD
8, 1673–1721, 2014

Table 4. Polynomial fit coefficients and weights used for the Greenland uncertainty grid.

Coefficient	Slope	SD	Roughness	*N*
C0	0.19	1.51	0.27	114.34
C1	−1.03	−1.03	−2.08	−11.57
C2	−5.89	0.22	11.89	0.49
C3	121.00	−0.02	−10.16	−0.01
C4	−286.00	7.6×10^{4}	3.9	1.4×10^{4}
C5	284.26	-1.8×10^{5}	−0.78	-1.09×10^{6}
C6	−137.62	2.3×10^{7}	0.08	5.02×10^{9}
C7	32.25	-1.5×10^{9}	-4.7×10^{3}	-1.3×10^{11}
C8	−2.94	4.2×10^{12}	1.1×10^{4}	1.3×10^{14}
Weights	0.26	0.24	0.34	0.16

TCD
8, 1673–1721, 2014

Table 5. Polynomial fit coefficients and weights used for the Antarctica uncertainty grid.

Coefficient	Slope	SD	Roughness	*N*
C0	0.38	0.29	0.15	70.95
C1	−7.94	−0.41	−1.11	0.19
C2	67.26	1.58	10.59	-2.3×10^{3}
C3	−117.11	−0.71	−12.17	6.6×10^{6}
C4	98.46	0.14	3.9	-9.4×10^{9}
C5	−44.68	−0.015	−1.96	7.5×10^{12}
C6	12.5	9.0×10^{4}	0.32	-3.5×10^{15}
C7	−2.17	-2.8×10^{5}	−0.03	8.7×10^{19}
C8	0.18	3.5×10^{7}	9.2×10^{4}	9.1×10^{23}
Weights	0.27	0.15	0.49	0.09

TCD
8, 1673–1721, 2014

Table 6. ICESat inter-campaign offset (LC) determined in Ewert et al. (2012) updated for release 33.

LC	Bias (m)	LC	Bias (m)
1A	+0.068	3F	+0.01
2A	+0.009	3G	−0.04
2A	+0.059	3H	−0.002
2B	+0.038	3I	−0.015
2C	−0.042	3J	−0.047
3A	+0.051	3K	−0.06
3B	+0.054	2D	−0.024
3C	+0.028	2E	−0.033
3D	−0.021	2F	−0.029
3E	−0.005		

TCD
8, 1673–1721, 2014

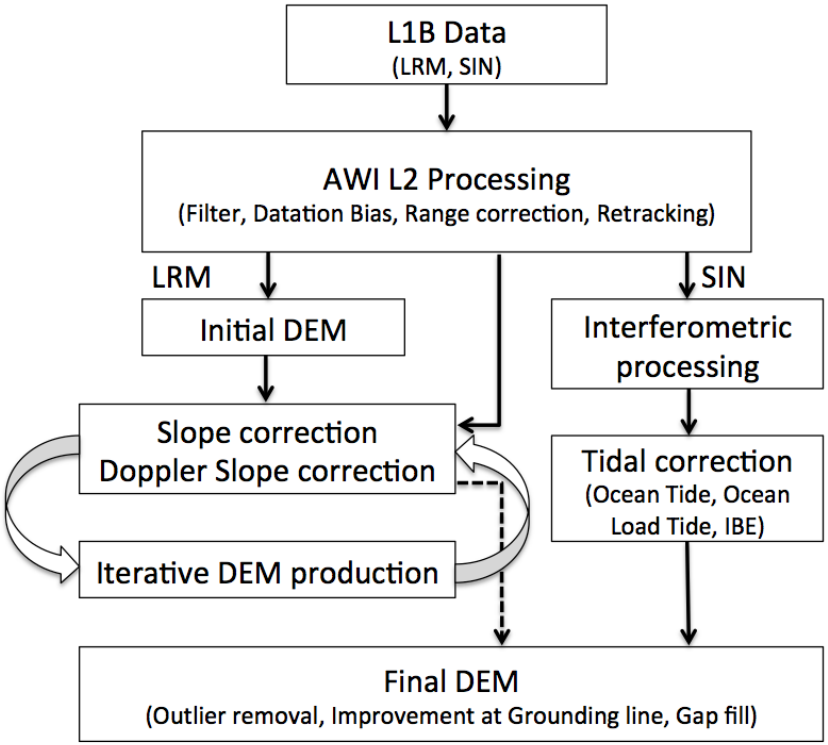

Fig. 1. Diagram of the processing scheme used to derive the final DEM.

TCD
8, 1673–1721, 2014

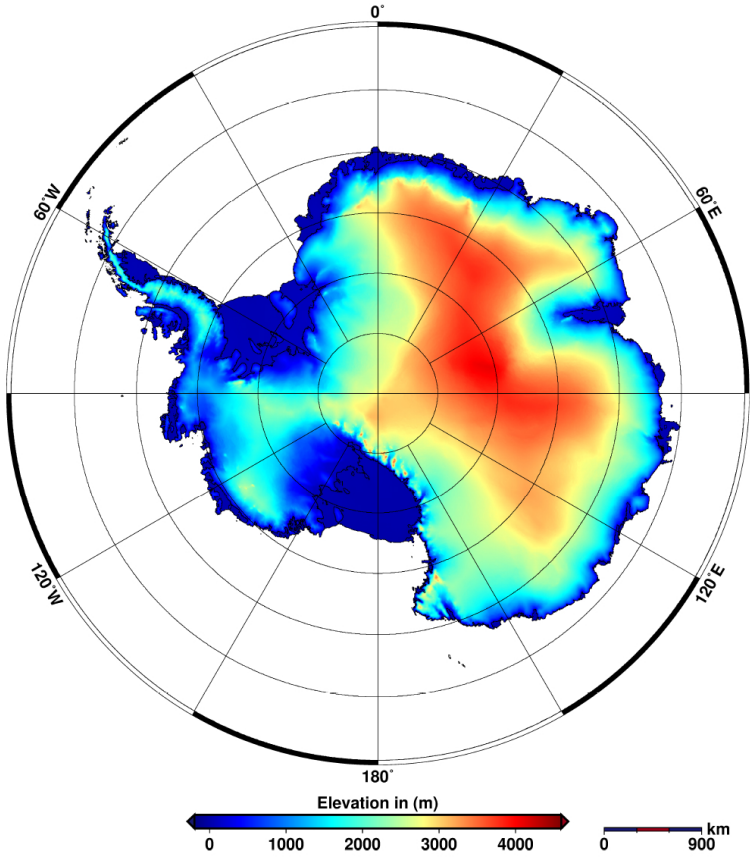

Fig. 2. New elevation model of Antarctica derived from CryoSat-2.

TCD
8, 1673–1721, 2014

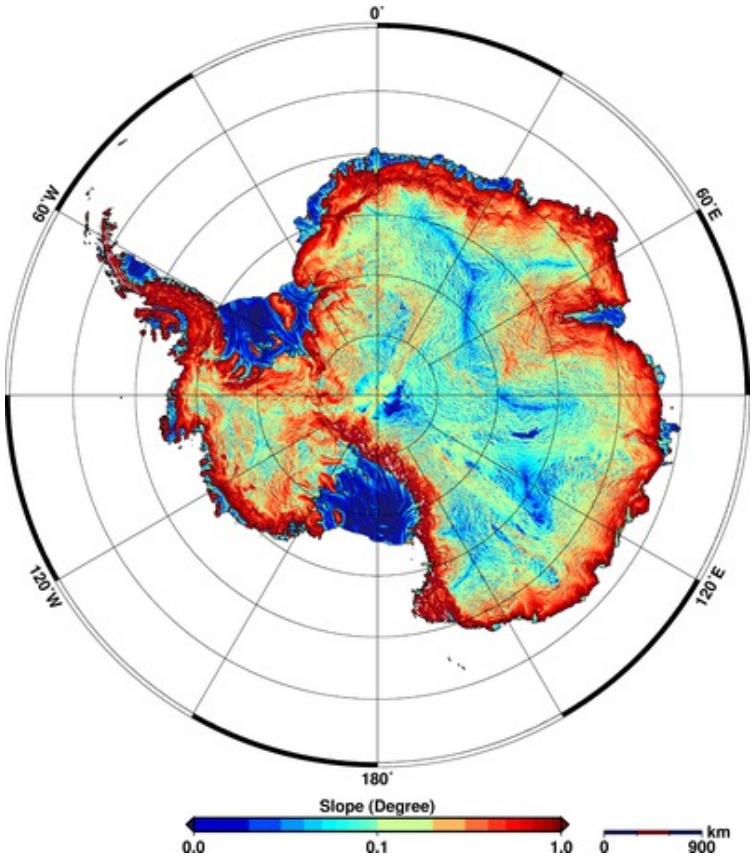

Fig. 3. Surface slopes, estimated from the new elevation model of Antarctica.

TCD
8, 1673–1721, 2014

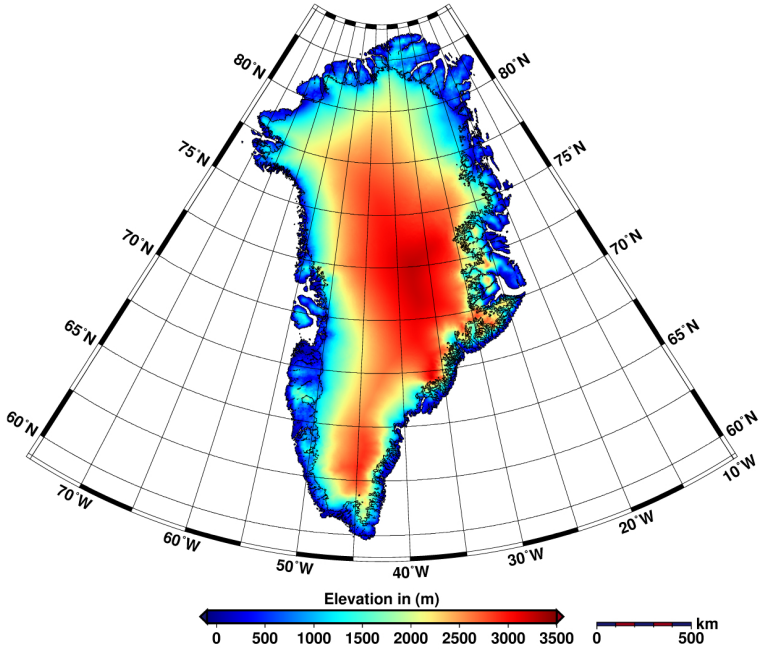

Fig. 4. New elevation model of Greenland derived from CryoSat-2.

TCD
8, 1673–1721, 2014

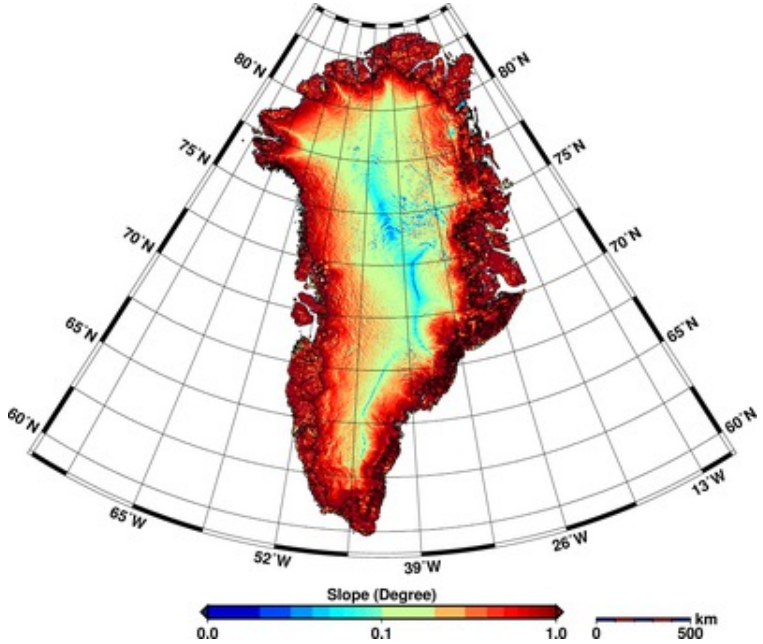

Fig. 5. Surface slopes, estimated from the new elevation model of Greenland.

TCD
8, 1673–1721, 2014

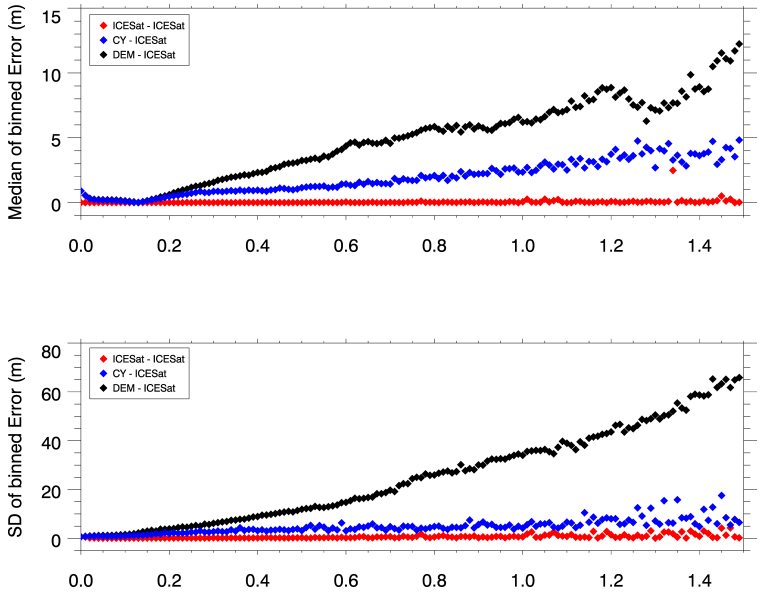

Fig. 6. Statistics of binned differences with respect to surface slope at a bin size of 0.01° for Antarctica. The upper panel shows the median of the binned differences and the lower panel its standard deviation. Red diamonds represent ICESat cross over differences, blue diamonds Cryosat/ICESat crossover differences and black diamonds the differences between the DEM and ICESat.

TCD
8, 1673–1721, 2014

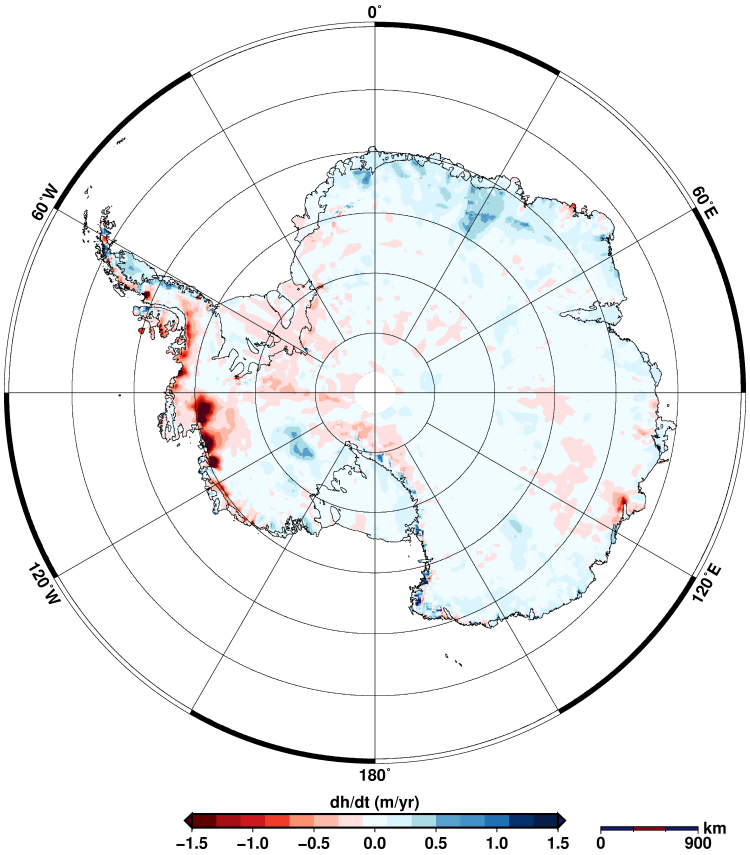

Fig. 7. Map of elevation change of Antarctica between 2011 and 2012 derived from along-track processing of two full CryoSat-2 cycles.

TCD
8, 1673–1721, 2014

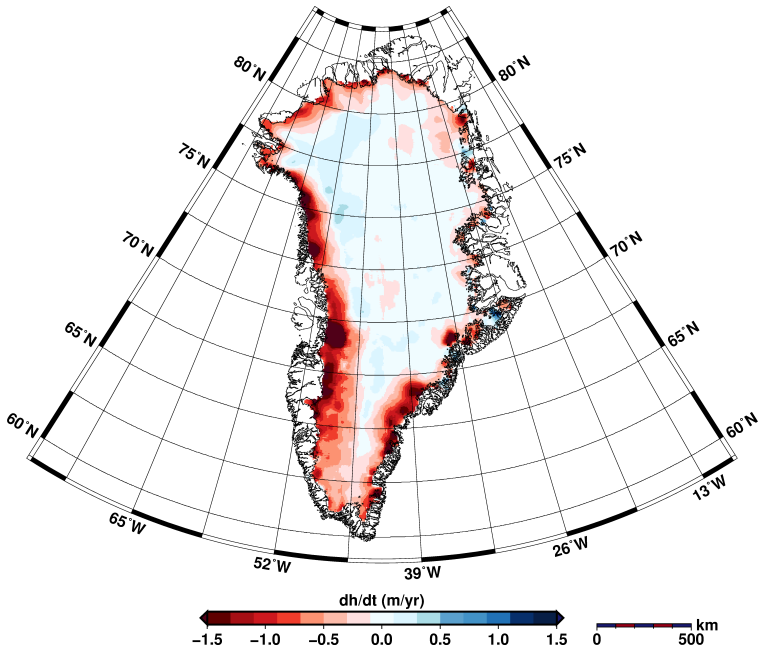

Fig. 8. Map of elevation change of Greenland between 2011 and 2012 derived from along-track processing of two full CryoSat-2 cycles.

TCD
8, 1673–1721, 2014

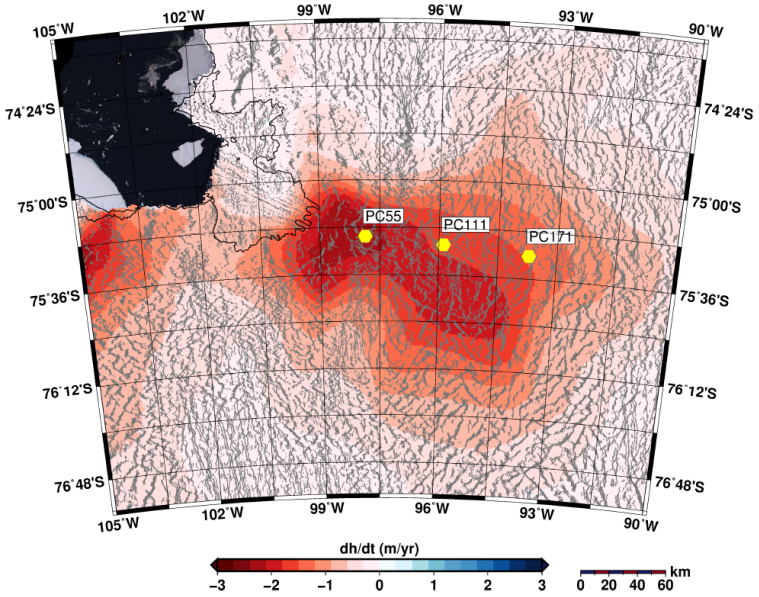

Fig. 9. Elevation change occurring at the Pine Island Glacier in West Antarctica. Data coverage of dh/dt measurements is shown for CryoSat (grey) and ICESat (black). The yellow hexagons represent the GPS sites in Scott et al. (2009)

TCD
8, 1673–1721, 2014

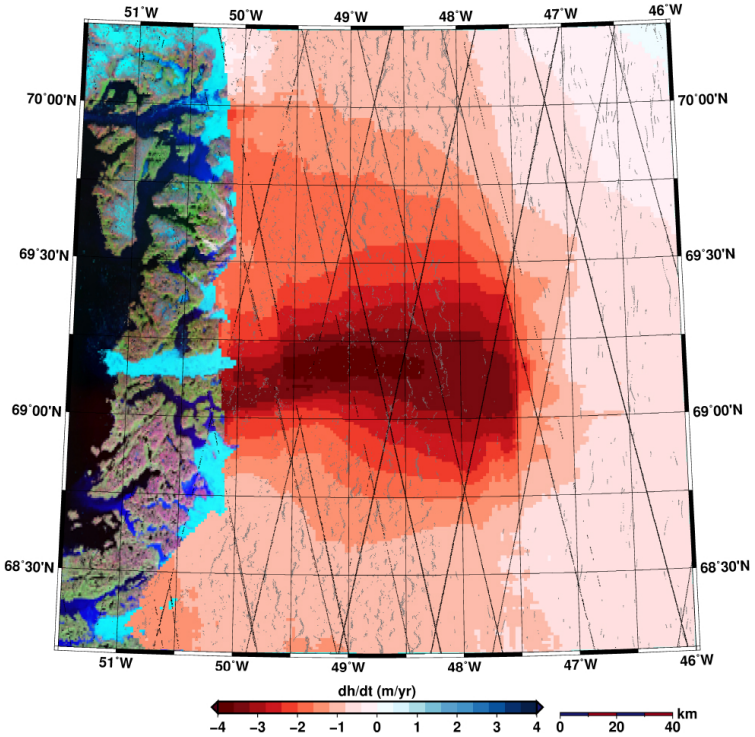

Fig. 10. Jakobshavn Isbræ is experiencing massive thinning of more than 4 m yr^{-1}. The thinning extends more than 250 km inland. Unfortunately, CryoSat-2 shows data loss in the catchment area of the glacier due to the high surface roughness. Data coverage is shown for CryoSat (grey) and ICESat (black).

TCD
8, 1673–1721, 2014

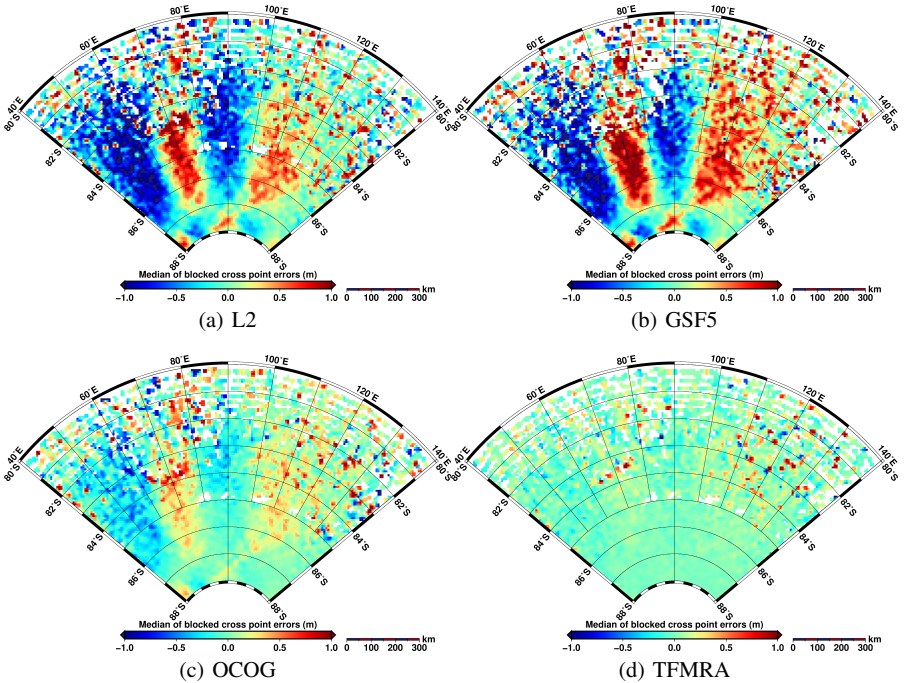

(a) L2 (b) GSF5

(c) OCOG (d) TFMRA

Fig. 11. Results of Baseline B LRM crossover analysis in East Antarctica using different re-trackers. Best results give the threshold first maxima re-tracker (TFMRA), with lowest standard deviations and strong suppression of the periodic pattern.

TCD
8, 1673–1721, 2014

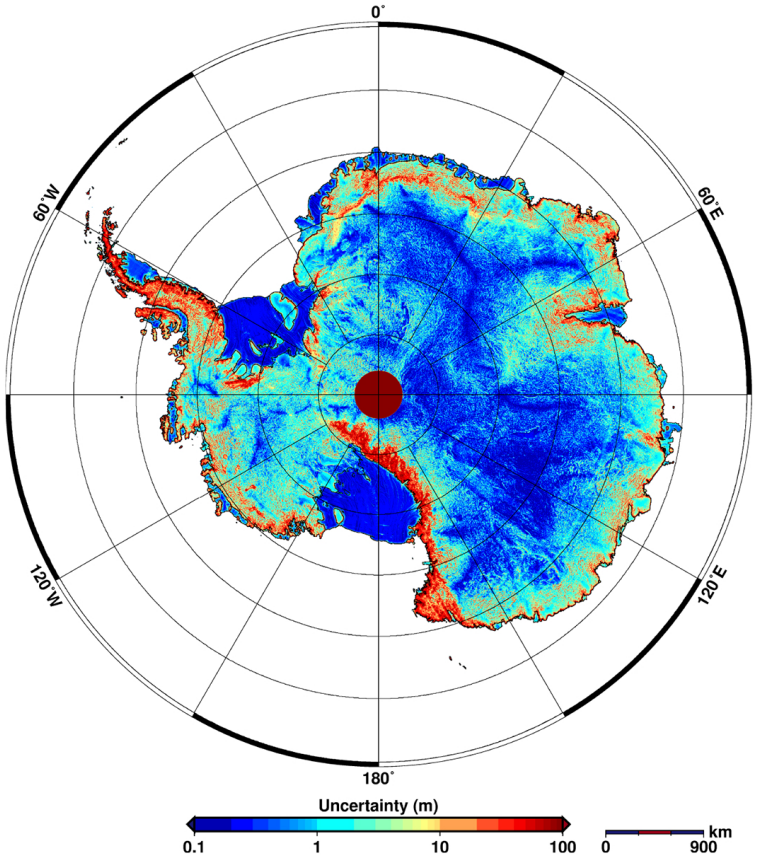

Fig. 12. Uncertainty map of the new Antarctica DEM calculated using a multiple regression approach based on DEM–ICESat differences.

TCD
8, 1673–1721, 2014

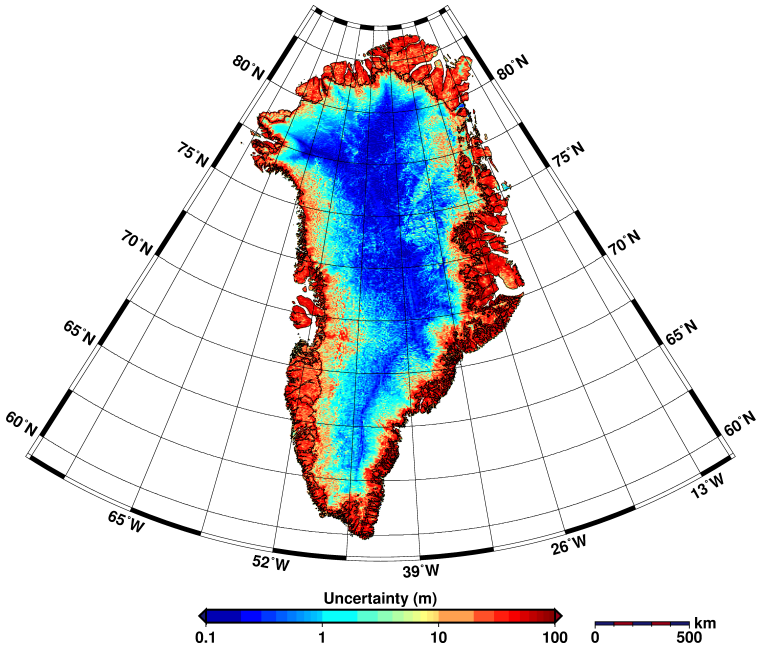

Fig. 13. Uncertainty map of the new Greenland DEM calculated using a multiple regression approach based on DEM–ICESat differences.

TCD
8, 1673–1721, 2014

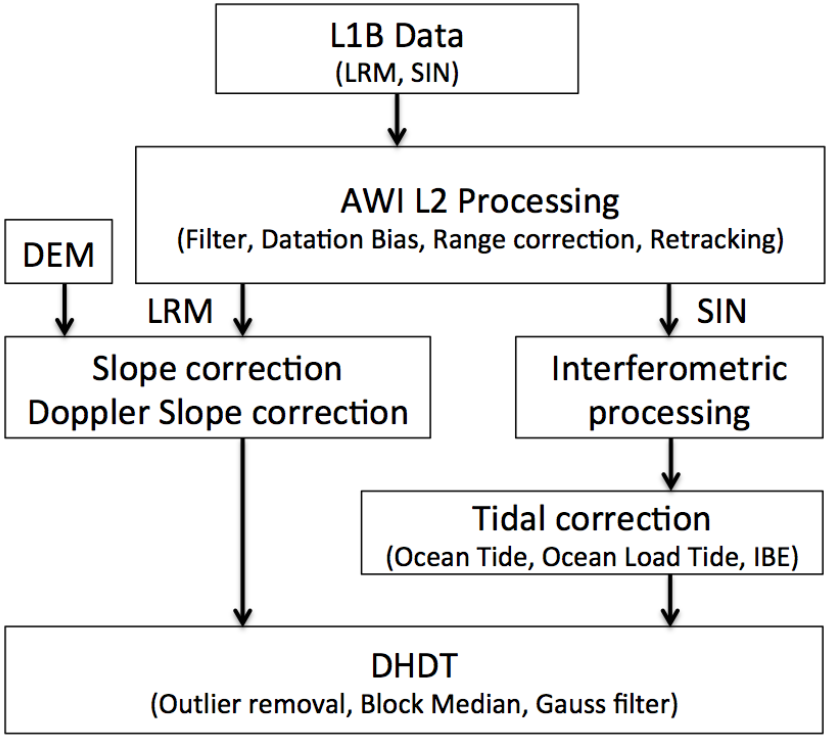

Fig. 14. Sketch of the processing scheme used to derive the final dh/dt map.

TCD
8, 1673–1721, 2014

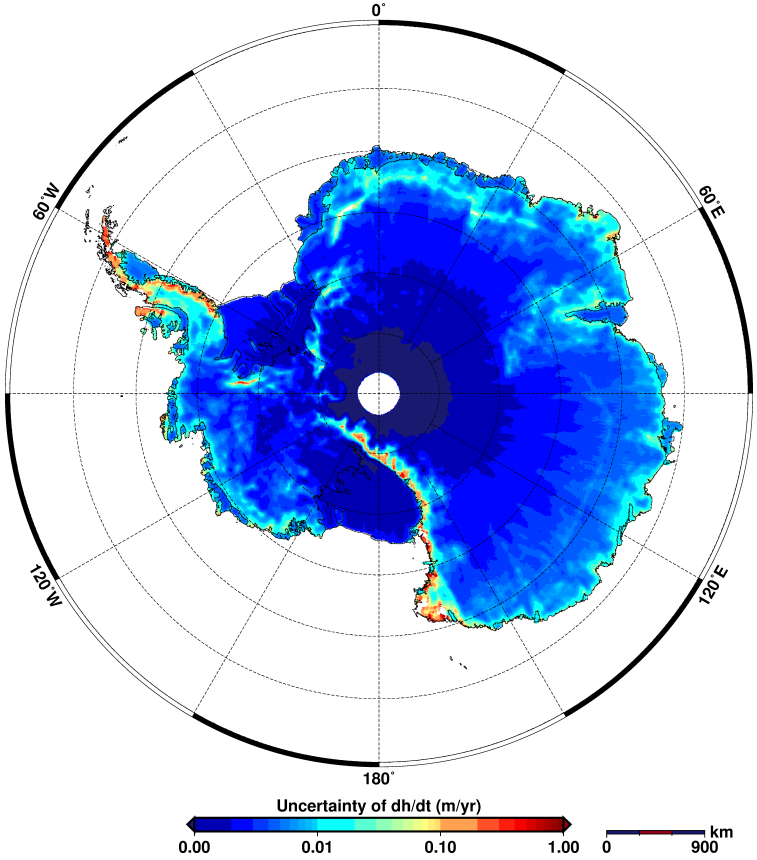

Fig. 15. Uncertainty map of elevation change of Antarctica derived from error propagation. Clearly indicated are the high uncertainties at the steep margins.

TCD
8, 1673–1721, 2014

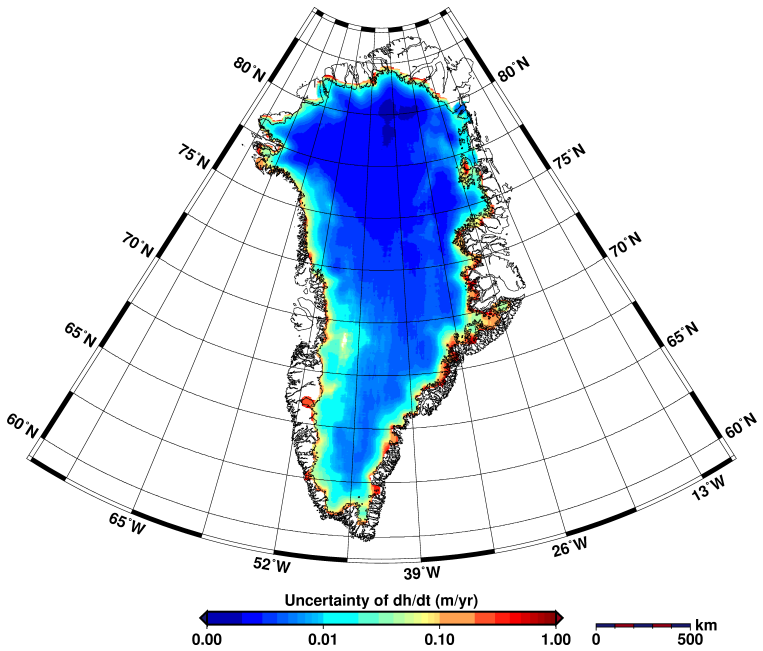

Fig. 16. Uncertainty map of elevation change of Greenland derived from error propagation. Clearly indicated are the high uncertainties at the steep margins.

TCD
8, 1673–1721, 2014